Received 27 May 2021; revised 25 June 2021; accepted 28 June 2021. Date of publication 5 July 2021; date of current version 15 July 2021.

Digital Object Identifier 10.1109/OJAP.2021.3094672

Stochastic Channel Parameters for Train-to-Train Communications

PAUL UNTERHUBER [1] (Member, IEEE), MICHAEL WALTER [1] (Senior Member, IEEE), UWE-CARSTEN FIEBIG [1] (Senior Member, IEEE), AND THOMAS KÜRNER [2] (Fellow, IEEE)

[1] Institute of Communications and Navigation, German Aerospace Center, 82234 Oberpfaffenhofen, Germany

[2] Institute for Communications Technology, Technische Universität Braunschweig, 38106 Braunschweig, Germany

CORRESPONDING AUTHOR: P. UNTERHUBER (e-mail: paul.unterhuber@dlr.de)

ABSTRACT The profound knowledge of radio wave propagation is essential for the design and test of wireless communication systems especially in demanding environments and for mobile transmitters and receivers. In this article we provide an accurate description of the relevant propagation parameters for train-to-train scenarios considering typical environments such as railway stations, open field and hilly terrain with cutting. At the beginning of this contribution we shortly describe the comprehensive train-to-train measurement campaign which is the basis for all further evaluations. We treat the stationarity of the channel in time and frequency and derive power delay profiles, and the Doppler spectral densities. Furthermore, distance-variant statistics about the *k*-factor, delay spread and Doppler frequency spread are presented. We show that these parameters change very much for different environments and distances. For all stochastic channel parameters we propose distance dependent model parameters.

INDEX TERMS High speed train, train-to-train propagation, non-stationarity, stochastic channel model, power delay profile, fading statistics, rms delay and Doppler frequency spread, *k*-factor, path loss model.

I. INTRODUCTION

RELIABLE train-to-train (T2T) communication is a key technology for the next generation of railway applications and control, and will enable the operation of new train concepts such as autonomously driving high speed trains and virtual coupling [1]. The virtual coupling of trains can be seen similar as platooning of cars or trucks on the highway. Virtual coupling will replace the electrical and mechanical coupling of trains with the consequence that trains and even individual wagons will travel at very short distances from each other. Data exchange and distance control will be possible via wireless communication between trains. Several projects like Roll2Rail and X2Rail within the European rail initiative Shift2Rail are focusing on virtual coupled trains and T2T communication [2].

In the last decades the research on T2T communication focused on products like a railway collision avoidance system based on terrestrial trunked radio [3]. Corresponding narrow band T2T channel models for the 400 MHz band were presented by [4] and [5]. More recently, with the growth of the intelligent transportation system (ITS) for road vehicles, the interest in novel railway applications and control has grown too and with it the need for enhanced train-to-ground (T2G) and novel T2T communication. In [6] and [7] Wang *et al.* investigated the use of T2T communication systems based on a modified 3GPP Long Term Evolution (LTE) cellular - vehicle to everything (C-V2X) communication standard for the communication-based train control system. The underlying channel models are based on T2G models or simple path loss models. Reference [8] presented T2T communication simulations based on the COST 207 suburban land-mobile channel model. The use of the IEEE 802.11p standard for T2T communications in railway environments was investigated with measurements in [9] and [10]. All publications lack a detailed T2T channel model as a basis for the studies. To the best of the authors' knowledge, no dedicated T2T channel model for frequencies above 1 GHz has been published to support the research on future T2T communications as already mentioned in [11].

In comparison to T2T communication a lot of research has been carried out in the field of T2G and car-to-car (C2C) communication. T2G channel models were introduced

in [12] for railway stations and in [13] for cross bridges. A T2G geometry-based stochastic channel model (GSCM) was presented in [14] and the influence of regularly appearing objects like overhead line masts on the channel was analyzed in [15]. Further work on T2G channel models is summarized in [16]–[19]. For C2C communication several measurement campaigns have been carried out in numerous environments and a variety of parameters have been analyzed: power delay profile (PDP) and Doppler spectral density (DSD) for overtaking and signal blocking scenarios [20], k-factor for urban, sub-urban and highway scenarios [21], and delay and Doppler frequency spreads for urban, sub-urban and highway [22]. Surveys on C2C channel models were presented in [23]–[26].

The above mentioned publications in the field of T2G and C2C communication state that reliable communication is only possible with a profound knowledge of the propagation channel. Whereas various T2G and C2C channel models already exist, measurement based wideband channel models for T2T communications are still missing. It is expected that T2T channels differ very much from C2C channels since T2T environments are very different from C2C environments. Furthermore we also expect T2G channels to differ significantly from T2T channels because both transmitter and receiver are moving in the latter case. Thus, neither T2G nor C2C channel models should be used for the modeling of T2T propagation.

Therefore, our research focuses on T2T channel modeling. We carried out a comprehensive channel measurement campaign in the framework of the Roll2Rail project using two high speed trains and the DLR RUSK channel sounder [27]. The recorded data sets encompass propagation data for the railway station, open field and hilly terrain with cutting environments. Based on these data sets, we analyze the time-variant behavior of the T2T propagation channel. First results for the path loss and shadow fading characteristics were published in [28]. The influence of railway infrastructure on T2T propagation was presented in [29] and [30].

The contribution of this paper can be summarized as follows.

- We analyze measurement data of three data sets representing typical railway environments and investigate the quasi-stationarity in time and frequency.
- We derive measurement based time-variant stochastic channel parameters for T2T communications in C-band for large and small scale fading. We present path loss and shadow fading analysis as well as Rician k-factor, root mean square (rms) delay spread and rms Doppler frequency spread estimates.
- We provide models for the statistical distribution of distance dependent channel parameters for the above mentioned environments for distances from 10 m to 1000 m.

The paper is organized as follows. In Section II we shortly present the channel measurement campaign encompassing the measurement equipment, covered scenarios and environments. As basis for all further evaluations, we analyze the measurement data, resume the stationarity assumptions, reveal to which extent the stationarity of the channel is violated and discuss the PDP and DSD in Section III. Starting with a concise derivation of large scale and small scale fading parameters, we show statistics on the path loss (PL), shadow fading, k-factor, delay spread and Doppler frequency spread in Section IV. Thus, we give a detailed insight into the stochastic behavior of the T2T channel for three typical railway environments. The conclusion, i.e., Section V completes the paper.

II. CHANNEL MEASUREMENT CAMPAIGN

In this section we briefly summarize the channel measurement campaign. A detailed description about the DLR RUSK channel sounder can be found in [27] and about the measurement campaign in [31].

A. MEASUREMENT EQUIPMENT AND SETUP

We performed the T2T channel measurement campaign with the DLR RUSK channel sounder in single-input single-output (SISO) mode at $f_c = 5.2\,\text{GHz}$ and a bandwidth of $B = 120\,\text{MHz}$. For synchronization purpose the sounder consists of Rubidium frequency normals at the transmitter (Tx) and receiver (Rx) side. The data was collected with a snapshot rate of $t_s = 1.024\,\text{ms}$ and a maximum excess delay of $t_p = 12.8\mu s$. The setting summarized in Table 1 leads to a maximum alias free Doppler frequency resolution of $\nu_{max} = \pm 488\,\text{Hz}$ and a maximum resolvable path length of $d_{max} = 3.8\,\text{km}$. The maximum equivalent isotropically radiated power (EIRP) was set to 33 dBm. Prior to every measurement run, a calibration measurement was performed including all parts of the channel sounder, connectors and cables except the antennas.

Measurements with trains on electrified tracks underlie strict limitations. The equipment mounted outside of the train, and this includes the antennas on the roof, needs to be certified for rolling stock. On each train we used omni-directional Huber&Suhner SWA-0859/360/4/0/DFRX30_2 antennas. As shown in Fig. 1 we assume the T2T propagation within a horizontal plane. We have detected that the interaction points of reflected and scattered signals at railway infrastructure like buildings, masts or bridges are mainly at the same height. Furthermore, the antennas on both trains are mounted on the same height. Hence, we assume an omni-directional pattern with an azimuth antenna gain of $G_T = G_R = 6\,\text{dBi}$ as provided by [32]. Due to the SISO measurement setup we can not derive angular information for multipath components (MPCs) and therefore, we can not take the antenna pattern into account for multipath analysis. In the following analysis we treat the antenna as part of the wireless channel. In a previous analysis focusing on the line of sight (LOS) signal power estimation and resulting PL models the antenna pattern was taken into account [28].

Even though we would have liked to carry out the measurements on trains traveling on the same track at short

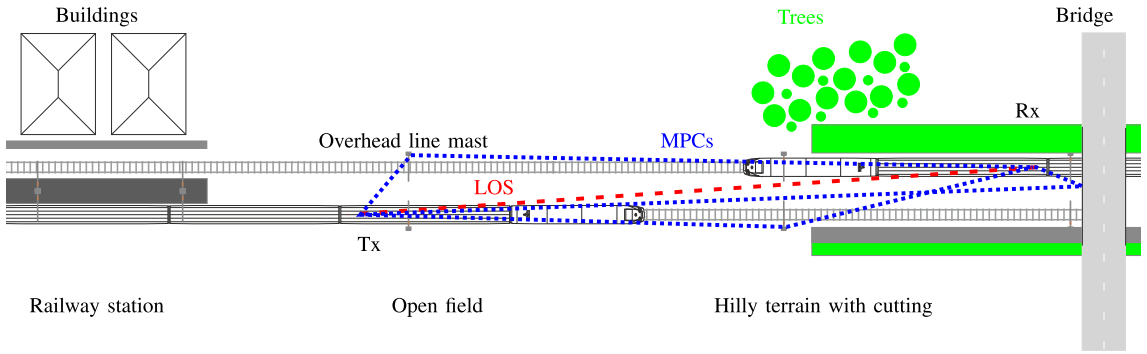

FIGURE 1. HSR environments with IOs and the resulting LOS path and MPCs for T2T communication.

TABLE 1. Channel sounder settings.

Parameter		Value
Center frequency	f_c	5.2 GHz
Bandwidth	B	120 MHz
Snapshot rate	t_s	1.024 ms
Excess delay	t_p	12.8 μs
Sub carriers	Q	1537
EIRP		33 dBm

distances, for safety reason we had to perform our measurements with two trains driving on parallel tracks. We performed several maneuvers such as platooning, approaching or separation with different velocities which reflects maneuvers for the virtual coupling application.

B. SCENARIOS

We define a scenario as the combination of the environment and the maneuver performed by the involved trains. Since the two trains run on parallel tracks we have the freedom to perform overtaking maneuvers. Within an overtaking maneuver one train is catching up to another train as it would be the case for one train joining a platoon of virtual coupled trains. We measured the channel transfer function in several interesting scenarios: departure and arrival in a railway station, several overtakes in open field and hilly terrain with cutting environments.

To achieve high spatial resolution and to fulfill the maximum resolvable Doppler frequency constraints of the used channel sounder we performed the measurements with rather low velocities. If we consider virtually coupled trains driving with similar velocities, the relative velocity will be rather low and in the order of the relative velocities we have chosen for our scenarios. The influence of MPCs caused by interacting objects (IOs) on the T2T communication performance is an important aspect as we present in the following sections. Nevertheless, we could learn from similar measurement evaluations for T2G communications, that the influence of the velocity is negligible for stochastic parameters; only the Doppler frequency shift is related to the velocity and can be seen as a scaling factor [33].

In the railway station environment, one train was standing on the platform and the other train departed and accelerated from 0 km/h to 50 km/h and, later, arrived and decelerated from 50 km/h to 0 km/h. Outside the railway station the Tx train was constantly driving with a velocity $v_T = 50$ km/h. The Rx train was either driving $v_R = 10$ km/h if it was in front of Tx train or $v_R = 70$ km/h if it was behind the Tx train.

C. ENVIRONMENT AND TRACK ARCHITECTURE

The high speed track between the station Roma Termini and station Napoli Centrale has a length of 205 km. The biggest share of the track runs through open field and hilly terrain environment. In contrast to open field with negligible IOs apart from the railway infrastructure, hilly terrain with cutting is characterized by frequently occurring cuttings with embankments or walls. Several tunnels with an accumulated length of 39 km exist between Naples and Rome. Based on a track analysis the following environments have been identified: railway station, open field, hilly terrain and tunnel. Certainly the tunnel environment has a significant influence on the propagation characteristics. In comparison to the other three environments, the tunnel environment has to be analyzed in more detail and is out of scope within this publication. Hence, all evaluations and the resulting models are split into the environments railway station, open field and hilly terrain with cutting. Typical views seen from the driver's compartment are shown in Fig. 2.

Besides the environment, the track architecture itself influences the wireless propagation significantly. The minimum curve radius for high speed railways (HSRs) is in the range of several kilometers. This large curve radius and rather straight track sections lead to the situation that LOS is often ensured over large distances. Typical objects along the track are overhead line masts, cross bridges, buildings or other trains. Fig. 1 shows the geometry of these objects; for distances between Tx and Rx up to $d_{TR} = 1$ km, mainly overhead line masts and cross bridges cause MPCs. The overhead line masts appear regularly with a maximum spacing of 60 m. In contrast cross bridges and other trains occur sparsely. By increasing the distance between the two trains to more than 1 km non-LOS (NLOS) conditions may occur due to blocking by large buildings and hills.

(a) Railway station.

(b) Open field.

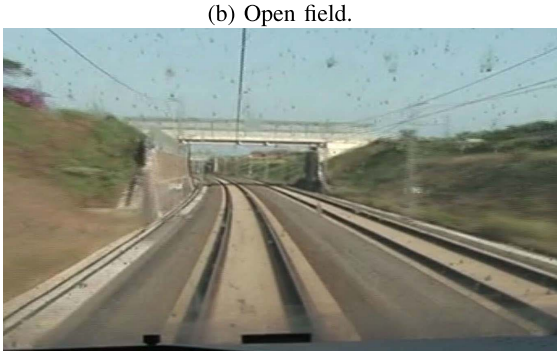

(c) Hilly terrain with cutting.

FIGURE 2. Views of the environments seen from the driver's compartment [34].

III. ANALYSIS OF THE MEASUREMENT DATA

Our analysis is based on three data sets: The first data set represents one train standing and one train departing or arriving in railway station environment. The second data set was recorded while the trains were driving with a relative velocity $\Delta v \approx 20\,\text{km/h}$ in an open field environment. The third data set was recorded half in open field and half in hilly terrain with cutting environment; the Tx train and the Rx train were driving with $\Delta v \approx 40\,\text{km/h}$

The measured propagation parameters recorded in mentioned data sets can be described with deterministic system functions. Assuming wide-sense stationary uncorrelated scattering (WSSUS) as introduced by [35] and extended by [36] we can derive the correlation functions and stochastic channel parameters [37]. The WSSUS assumption holds for stationary conditions like in cellular communication, but in a railway scenarios with moving Tx and Rx and large measurement bandwidth the assumption may be violated. Nevertheless, we can assume that the WSSUS assumption holds for quasi-stationarity regions in time and frequency [38].

A. FROM THE MEASURED TRANSFER FUNCTION TO THE ESTIMATED LOCAL SCATTERING FUNCTION

The DLR RUSK channel sounder records a snapshot based time-variant transfer function $H(t,f)$. By assuming quasi-stationarity we can apply an inverse discrete Fourier transform (iDFT) with a moving frequency window and express the time-variant impulse response $h(t,\tau)$ with the time instant t and delay τ. In the literature, $h(t,\tau)$ is often called channel impulse response (CIR) and can be expressed as

$$h(t,\tau) = \frac{1}{\sqrt{I}} \sum_{f=0}^{I-1} H(t,f)\mathrm{w}(f)\mathrm{e}^{j2\pi\tau f}, \tag{1}$$

with the window function $\mathrm{w}(f)$ and a window length of I bins. I defines the size of the quasi-stationarity region in frequency.

In a second step, the Doppler-variant impulse response $s(\nu,\tau)$, also known as spreading function, is derived by a windowed discrete Fourier transform (DFT) of the CIR as

$$s(\nu,\tau) = \frac{1}{\sqrt{J}} \sum_{t=0}^{J-1} h(t,\tau)\mathrm{w}(t)\mathrm{e}^{-j2\pi\nu t}. \tag{2}$$

The used time window $\mathrm{w}(t)$ is set to the length of J snapshots. J defines the size of the quasi-stationarity region in time. The optimal value for I and J are evaluated in Section III-B. The windows $\mathrm{w}(f)$ and $\mathrm{w}(t)$ are defined as Chebyshev windows as investigated in [39].

In [40] the local scattering function (LSF) was introduced as representation of the delay and Doppler frequency dispersion for time-variant non-WSSUS fading channels. By applying filter functions in time and frequency around a given time and frequency point (t,f) and ensuring stationarity within these regions, the local scattering function (LSF) can be derived as

$$P_s(\nu,\tau;t,f) = |s(\nu,\tau)|^2. \tag{3}$$

Exemplary LSFs for the hilly terrain with cutting environment are shown in Fig. 3 for three snapshots at $t = [15, 20, 25]$s. We can clearly see the time-variant behavior of the LOS signal and also the sparse but moving MPCs. We highlighted four MPCs as A, B, C and D in Fig. 3. For MPCs with a delay value close to the delay of the LOS signal, the MPCs experience a fast change of the Doppler frequency, whereas the delay changes slowly.

B. STATIONARITY ANALYSIS

As depicted in [40] we have to differentiate between stationarity regions and coherence regions. By assuming WSSUS, the coherence regions in time and frequency can be calculated. In other words, the coherence time T_{coh} and coherence bandwidth B_{coh} can be calculated based on the time correlation function $R_H(t)$ and the frequency correlation function

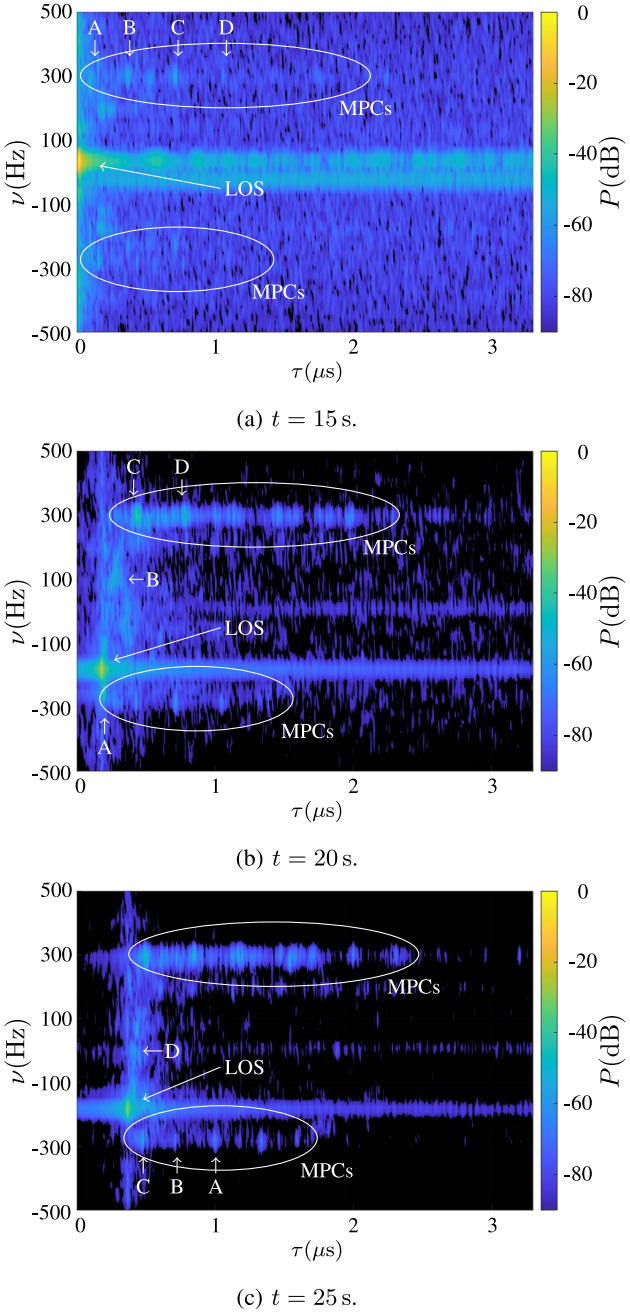

FIGURE 3. LSF for hilly terrain with cutting.

$R_H(f)$ respectively [37]. As we see in Section IV-C the delay spread σ_τ is based on the PDP and $R_H(f)$ is the Fourier transformed of the PDP, the rms delay spread σ_τ and B_{coh} have the well-known relation $B_{\text{coh}} \geq 1/(2\pi\sigma_\tau)$. Similar, the DSD is the inverse Fourier transform of $R_H(t)$ and following the rms Doppler frequency spread σ_ν and T_{coh} have the relation $T_{\text{coh}} \geq 1/(2\pi\sigma_\nu)$ [41].

We analyze the size of the quasi-stationarity regions in time t_{stat} and frequency f_{stat}. A definition of quasi-stationarity and a comparison between different methods to characterize the quasi-stationarity regions is presented by [38]. A common approach in the literature is to set the minimum time window between tenfold to hundredfold of the wavelength with respect to the relative velocity [42]. This results in $t_{\text{stat,min}} = 10\lambda/|\Delta\boldsymbol{\nu}_{\max}|$ with the maximum relative velocity $\Delta\boldsymbol{\nu}_{\max}$ and a wavelength $\lambda = c/f_c$, where c denotes the speed of light. In the railway station environment we used a maximum relative velocity between Tx and Rx of 50 km/h as Rx train was standing at the platform and Tx train was departing from the platform. This leads to a minimum stationarity time $t_{\text{stat,min}} = 32.8$ ms.

Different approaches were proposed in [42]–[44] to analyze the uncorrelated scattering (US) assumption. The quasi-stationarity frequency window can be roughly estimated by $f_{\text{stat,min}} = c/w_{\max}$ with a maximum width $w_{\max}$ of an IO [42]. Analyzing the IOs along a railway track, the maximum width of an overhead line masts, a tree or the reflecting phase of a building or cross bridge is not exceeding 30 m. This leads to a preliminary frequency window $f_{\text{stat,min}} = 10$ MHz. In [43] the authors argue with a small bandwidth to carrier frequency relation in combination with a low voltage standing wave ratio over the whole bandwidth B to assume US. In our case the relation results in 2.3 %. In [44] the authors state, that if $B << fc$ and $|f| = B/2$ they result in $(f_c - f)/f_c \approx 1$ and therefore they assume, that a fairly weak non-stationarity characteristic over the measurement bandwidth B occurs. Following the argumentation, they assume US.

To obtain more precession with respect to stationarity regions in time and frequency, we perform a stationarity analysis based on the LSF. We estimate the similarity between the LSF $P_s(\nu, \tau; t, f)$ at frequency instant f with $P_s(\nu, \tau; t, f + \Delta f)$ for $\Delta f \in [0, B]$. The time t is fixed for the frequency evaluation. Analogously, we estimate the similarity between the LSF $P_s(\nu, \tau; t, f)$ at time instant t, the previous and following LSFs $P_s(\nu, \tau; t + \Delta t, f)$ with $\Delta t \in [0, t]$. In this case, the frequency f is fixed. How similar the LSFs are, is measured by the collinearity. In [45] the collinearity was derived based on the correlation distance matrix for cellular communication and followed by [43] and [46] for C2C communication. The correlation distance or temporal correlation coefficient is hard to compare if both Tx and Rx are moving. Hence, the correlation distance was reformulated and applied to the power spectral density. The collinearity is a bounded metric $\text{col}\{P_s(\nu, \tau; t, f)\} \in [0, 1]$. If the LSFs are similar, the collinearity will taken on a value close to one. Or, if the LSFs vary strongly, the resulting value will be close to zero. The general form of the collinearity can be expressed as

$$\text{col}\{P_s(\nu, \tau; t, f)\}\big[g, g + \Delta g\big] = \frac{\sum_{\tau=0}^{\tau_{\max}} \sum_{\nu=-\nu_{\max}}^{\nu_{\max}} P_s(\nu, \tau; g) \odot P_s(\nu, \tau; g + \Delta g)}{\|P_s(\nu, \tau; g)\|_F \|P_s(\nu, \tau; g + \Delta g)\|_F}, \quad (4)$$

where $\|\cdot\|_F$ denotes the Frobenius norm. The variable $g \in \{f, t\}$ stands either for t or for f, respecting wide-sense

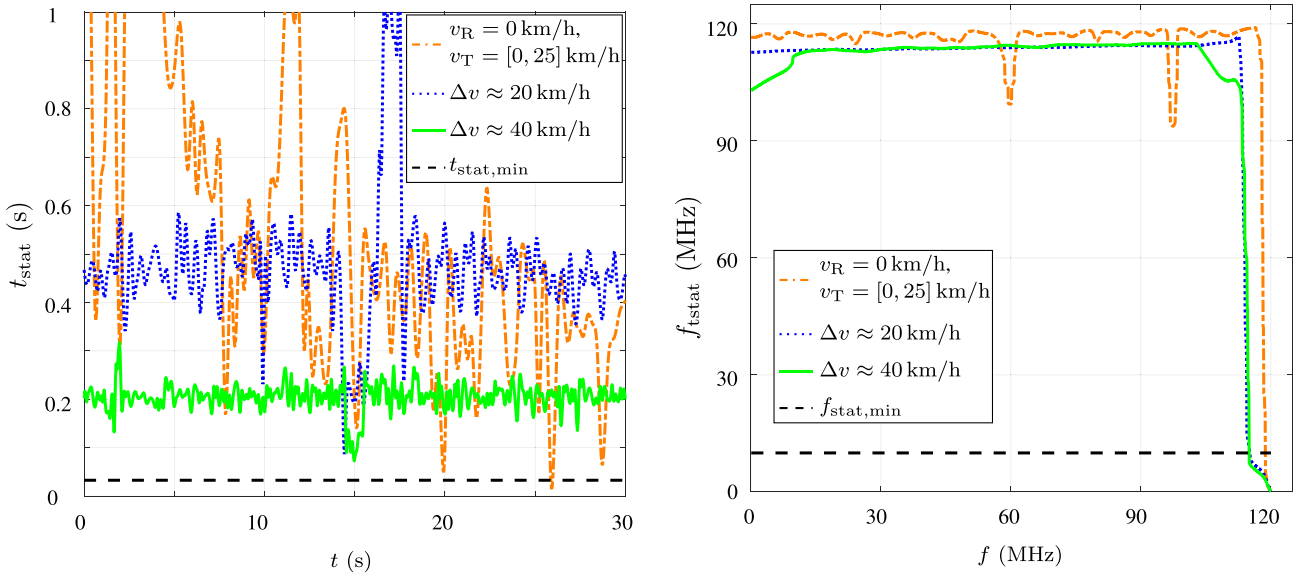

(a) Stationarity time.

(b) Stationarity frequency.

FIGURE 4. Stationarity for the different data sets. t_{stat} and f_{stat} are represented by the orange dash-dotted lines, the blue dotted lines and the green solid lines. Preliminary $t_{stat,min}$ and $f_{stat,min}$ are indicated as black dashed lines.

TABLE 2. Stationary time t_{stat} and stationary frequency f_{stat}.

Data set		J snapshots	t_{stat} ms	I bins	f_{stat} MHz
1: $v_R = 0\,km/h$, $v_T = [0, 25]\,km/h$	min	14	14.3	1201	93.8
	mean	555	568.3	1495	116.7
	used	64	65.5	1537	120
2: $\Delta v \approx 20\,km/h$	min	85	87.0	1444	112.7
	mean	461	472.1	1459	113.9
	used	64	65.5	1537	120
3: $\Delta v \approx 40\,km/h$	min	71	72.7	1319	103.0
	mean	200	204.8	1452	113.3
	used	64	65.5	1537	120

stationary (WSS) or US analysis. The collinearity analysis yields a symmetric matrix with the diagonal equal to one. The stationary time or frequency is the span around the diagonal, in which the values exceed a certain threshold; as in [42] and [47] we use a threshold $\alpha_{th} = 0.9$.

The band limitation of the measurement system leads to an underestimation of the stationarity time. The measurement bandwidth $B = 120\,MHz$ of our channel sounder results in a spatial resolution of 2.5 m. We translated the spatial resolution into time, by considering the velocities of the Tx and Rx. In this way we can eliminate this measurement artifact and obtain a realistic estimate of the stationarity time.

In Fig. 4(a) and Fig. 4(b) representative results for quasi-stationarity within the time window and the frequency range are plotted. The values for $t_{stat,min}$ and $f_{stat,min}$ are indicated as black dashed lines. We see, that the WSS assumption is fulfilled, but sporadic events with low t_{stat} occur. The US assumption is fulfilled for large frequency ranges for all environments. These results are in line with evaluations in the C2C domain performed by [43], [44], [47], [48].

For the first data set, t_{stat} indicated as orange dash-dotted line in Fig. 4(a) shows that the channel reveals high average stationarity even above 1 s and can be increased up to 65.5 ms. For the time from 30 s to 60 s, that is for higher velocity of the Tx, the analysis has some sporadic minimums with $t_{stat} = 14.3\,ms$. In Fig. 4(b) the stationarity analysis in the frequency domain shows a highly stationary behavior over the whole measurement bandwidth of 120 MHz.

The blue dotted line represents the second data set with $\Delta v \approx 20\,km/h$ resulting in t_{stat} varying from 87 ms to 1 s with an average value of 472.1 ms. The minimum stationarity time appear at $t = 15\,s$ as one train overtakes the other. Right after the crossing, around $t = 17\,s$ the t_{stat} reaches a peak. In this special case, the geometry of Tx, Rx and the IOs explains the peak. The distance between Tx and Rx is still small and at the same time, the surrounding IOs are far, because the Tx and Rx are in the middle of two overhead line masts. Due to the low velocity of the trains, the relation between a high LOS and low MPC signal power remains for around $t_{stat} = 1\,s$. The stationarity frequency f_{stat} shows a minimum of 112.7 MHz and a maximum of 117 MHz. Hence, for the further analysis we increase the stationarity windows to $t_{stat} = 65.5\,ms$ and $f_{stat} = 120\,MHz$ for the second data set.

The third data set recorded with $\Delta v \approx 40\,km/h$ results in an mean $\bar{t}_{stat} = 204.8\,ms$ with a minimum t_{stat} of 72.7 ms at $t = 15\,s$ shown as green solid line in Fig. 4(a). The shortest stationarity time appears at the time of the overtake maneuver. The stationarity in the frequency domain varies from 103 MHz up to 115 MHz for low and high bandwidth, but follows the same trend as the stationarity for other data sets. Hence, we set $t_{stat} = 65.5\,ms$ and $f_{stat} = 120\,MHz$.

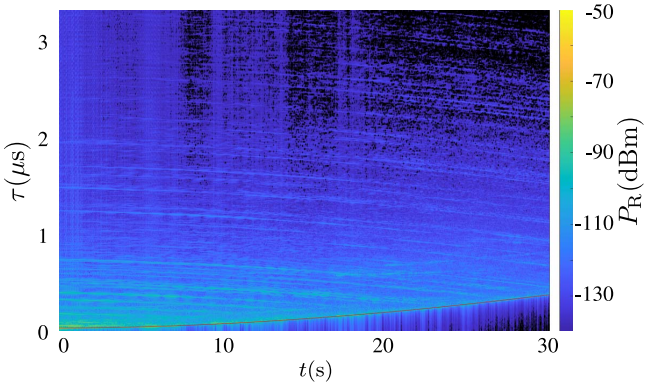

(a) Data set 1.

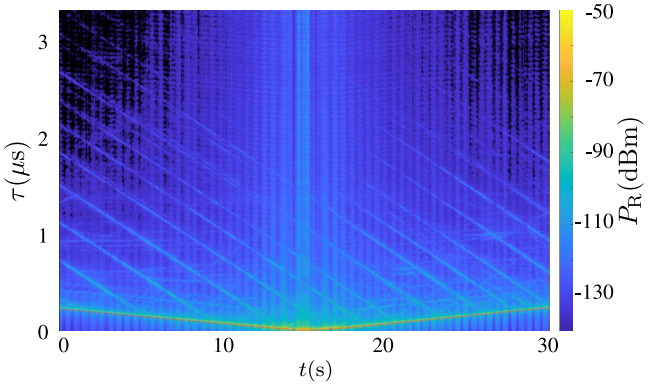

(b) Data set 2.

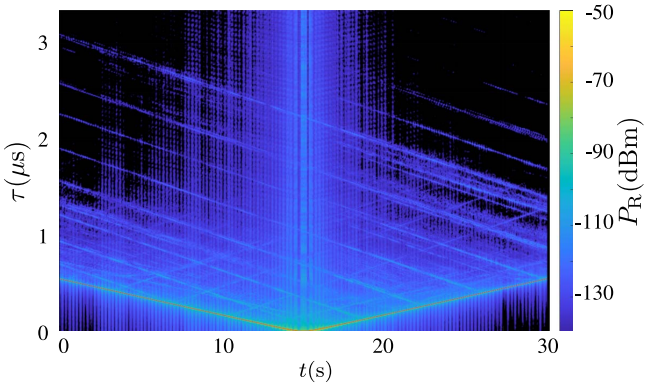

(c) Data set 3.

FIGURE 5. PDPs and GNSS based hypothetical LOS signal delay (red solid line) for the different data sets.

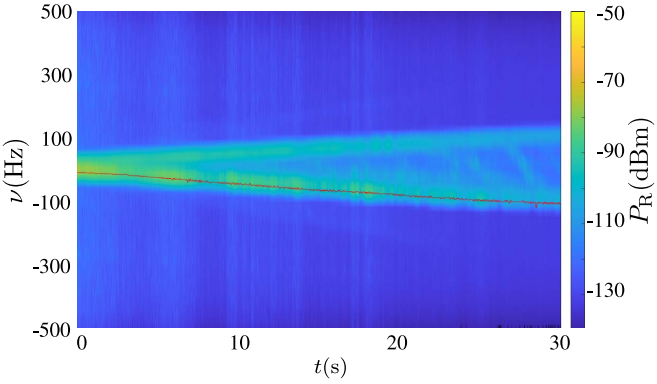

(a) Data set 1.

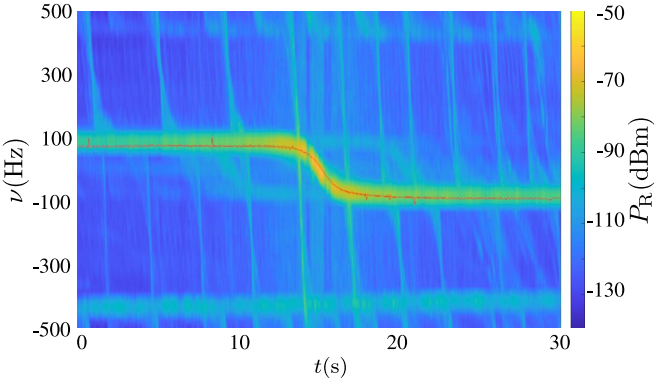

(b) Data set 2.

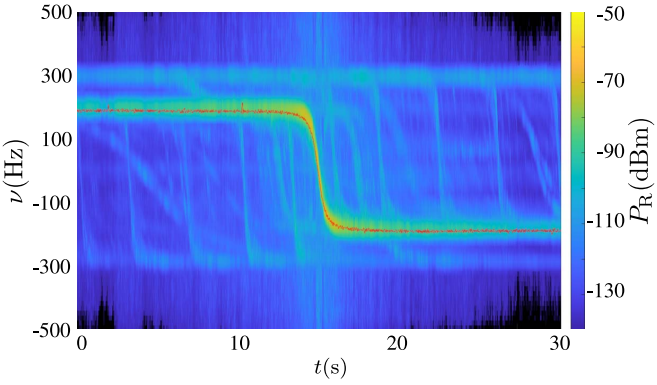

(c) Data set 3.

FIGURE 6. DSDs and GNSS based hypothetical LOS signal Doppler frequency (red solid line) for the different data sets.

It is worth noting, that the quasi-stationarity regions can vary with time as described in [43]. As we clearly see, the t_{stat} vary based on the relative velocity too. With increasing relative velocity, the quasi-stationarity region decreases over time correspondingly. Similar, the relation between the mean values of t_{stat} for the second and third data set correspond to the relation of the mean relative velocities of 20 km/h and 40 km/h, respectively. The higher relative velocity results into a lower mean t_{stat} because the vehicles cover different distances within the same time.

As a result of the stationarity analysis, the stationary time and frequency can be increased in comparison to the preliminary values $t_{\text{stat,min}}$ and $f_{\text{stat,min}}$. Even though the WSS assumption with $t_{\text{stat}} = 65.5$ ms is partially violated in the first data set, we chose this value to ensure a reasonable Doppler frequency resolution of 15.26 Hz. The stationary frequency window can be enlarged to the maximum bandwidth and US can be assumed for the T2T measurements; using $f_{\text{stat}} = 120$ MHz results in a delay resolution of 8.33 ns. The estimated minimum, mean and finally used values for t_{stat} with the related number of snapshots J and f_{stat} with the related number of frequency bins I are listed in Table 2.

C. POWER DELAY PROFILE AND DOPPLER SPECTRAL DENSITY

In this section we derive the time-variant PDPs and the time-variant DSDs from the LSF. As US can be assumed, the LSF can be reduced from a time-frequency varying function $P_s(\nu, \tau; t, f)$ to a time varying function $P_s(\nu, \tau; t)$. If not stated otherwise, the notations PDP and DSD consider a temporal variation of the functions. Both, the PDP and the DSD show the large variability and the fading behavior. The PDP reflects nicely the geometry of the Tx, Rx and IOs

$$P_h(\tau; t) = \frac{1}{J} \sum_{\nu=-J/2}^{J/2-1} P_s(\nu, \tau; t). \tag{5}$$

The DSD illustrates the movement of the Tx and Rx within the measurement

$$P_S(\nu; t) = \frac{1}{I} \sum_{\tau=0}^{I-1} P_s(\nu, \tau; t). \tag{6}$$

The PDPs and DSDs are plotted in Fig. 5 and in Fig. 6. For all three data sets we chose a sequence of 30 s; the red line indicates the GNSS based hypothetical LOS signal delay or LOS signal Doppler frequency. In the first data set we have a fixed configuration with standing Tx and Rx trains. At $t = 2$ s the Tx train starts moving while the Rx train is at still stand in the railway station. In the second data set the Rx train drives with a speed of 70 km/h and overtakes the Tx train which is driving with 50 km/h in open field environment. Data set three shows an overtaking maneuver with $v_T = 50$ km/h and $v_R = 10$ km/h. Till $t = 14$ s the maneuver was in an open field environment. Later the trains enter a cutting. In both, the second and third data set, the overtaking happens at $t = 15$ s with a minimum distance $d_{TR} = 5$ m.

Analyzing the PDPs of all three data sets we clearly see a regular pattern of MPCs. The amount of pronounced MPCs per snapshot varies between 14 to 20. The infrastructure of an electrified HSR mainly consists of overhead line system, where the masts are placed with a maximum spacing of 60 m. The spacing between the MPCs in Fig. 5(b) and Fig. 5(c) varies between 55 m and 59 m. Hence, we have a very strong indication that regularly appearing strong MPCs are caused by the overhead line masts. By passing an IO like an overhead line mast with the first train, the emitted MPC falls into the same delay bin as the LOS signal and superimposes to the LOS signal. The resulting signal may exhibit fading with respect to the LOS signal. After the second train passes the IO the delay of the MPC increases and the MPC can be differentiated again from the LOS signal. This behavior results in a average life time of MPCs of 45 s. Buildings, cross bridges and other IOs along the track cause also MPCs similar as the overhead line supports, but they do not appear in a regular manner. Furthermore, we can observe MPCs with a constant delay offset to the LOS signal over the whole measurement time in all three data sets. The delay offset of the detected MPCs is $\Delta\tau = [91.6, 183.3, 258.3]$ns; these delay offsets result in an additional path distance of $\Delta d = [27.46, 54.95, 77.43]$m and can be allocate to equipment mounted on the train roof as the pantograph and further distanced antennas.

The second data set shows a regular pattern of pronounced MPCs. Those pronounced MPCs occur in the third data set as well, but the MPCs and LOS signal experience stronger fading. In our evaluation the MPC richest propagation environment is the first data set in the railway station environment. In the railway station environment close platform roofs, other trains, masts and signs scatter the signals.

The corresponding DSDs are plotted in Fig. 6. In all three data sets MPCs yield a regular pattern although it looks different to the one of the PDP plots. Depending on the relative velocity of Tx and Rx the Doppler frequency of the LOS signal starts at $\nu = [0, 100, 200]$Hz for data set $[1, 2, 3]$, respectively. In all three plots the red solid lines represent the hypothetical Doppler frequency based on the relative velocity estimated from GNSS data. The instantaneous Doppler frequency can be calculated as $\nu_{GNSS}(t) = \cos(\alpha)|\Delta \boldsymbol{v}(t)|f_c/c$, with $\cos(\alpha) = 1$ for the LOS path.

In the first data set, the Tx accelerates up to 50 km/h, while the Rx remains at the platform of the railway station. This leads to the negative increase of the Doppler frequency of the LOS signal over time. MPCs coming from reflectors or scatterers towards which the Tx is driving are causing a positive increase in Doppler frequency. At the time as Tx passes the IO, the corresponding MPC changes the Doppler frequency from positive to negative.

In the second and third data set a similar behavior of the Doppler frequency can be observed. In both an overtake maneuver was performed and as a result the Doppler frequency of the LOS signal changes at $t = 15$ s from positive to negative, when the Tx passes the Rx or vice versa. In the same way as in for data set one, the Doppler frequency caused by an IO in front of one train, changes rapidly when the first train passes the IO to a value close to the Doppler frequency of the LOS signal. When the second train passes the IO, the Doppler frequency changes again to a higher negative value.

Due to the higher absolute velocity for Tx and Rx in the second data set, the Doppler frequency of IOs in front or in back of both trains can not be fully resolved. Hence, we observe an aliasing effect in Fig. 6(b) at $\nu = 450$ Hz and $\nu = -400$ Hz. The measurements in the third data set were performed with lower absolute velocities and therefore, the resulting Doppler frequency of all MPCs can be resolved at $\nu = \pm 300$ Hz. Hence, for the estimation of the small scale fading parameters in Section IV only data set three is used.

IV. TIME-VARIANT STOCHASTIC CHANNEL MODEL PARAMETERS

In this section we derive time-variant stochastic channel model parameters based on the analyzed measurement data. The large scale fading is described by the PL and shadow fading behavior of the wireless channel. The analyzed small

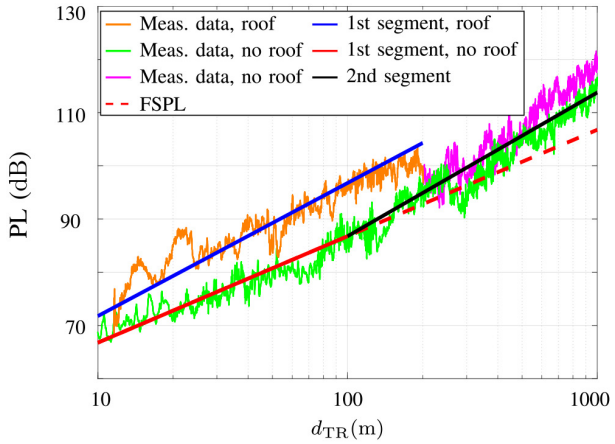

(a) Railway station.

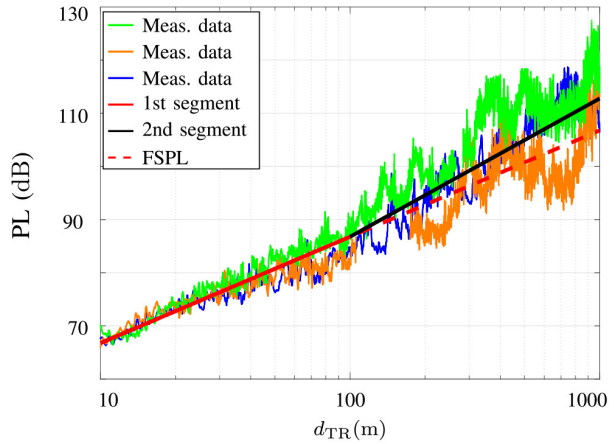

(b) Open field.

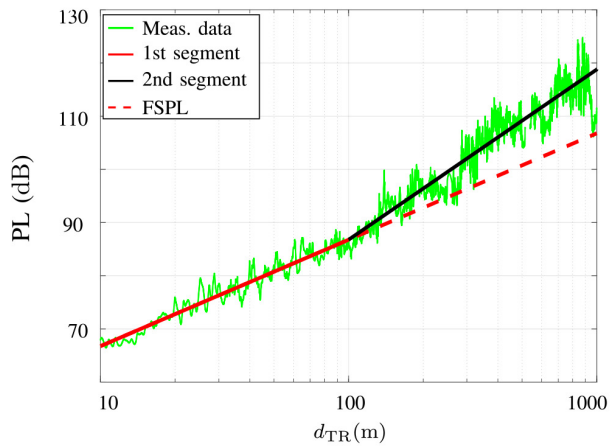

(c) Hilly terrain with cutting.

FIGURE 7. PL for railway environments. The green and orange lines represent the PL from measurement data. The blue and red lines represent the first segment, the black lines the second segment of the two-slope log-distance PL models. The red dashed lines mark the FSPL in each environment.

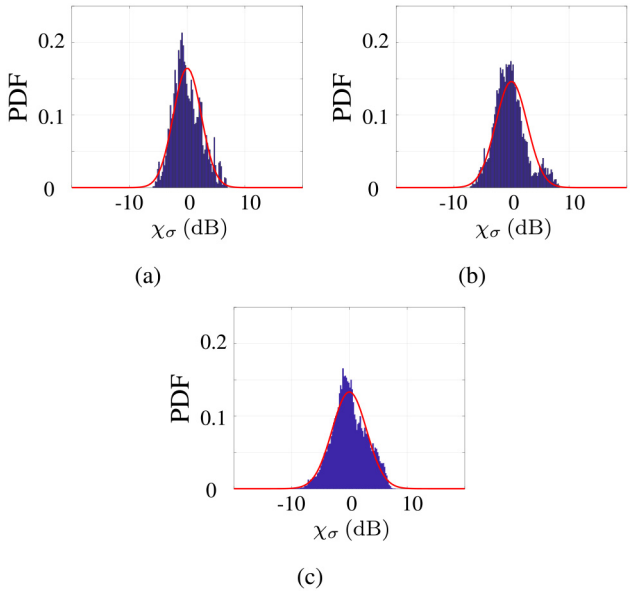

FIGURE 8. Log-normal shadow distribution for the first segment of the two-slope PL model for the railway station environments (a) without platform roof and (b) with platform roof. (c) shows the log-normal shadow distribution for the second segment. The blue histogram indicates the PDF of the measurement data and the red line the fitted Gaussian distribution.

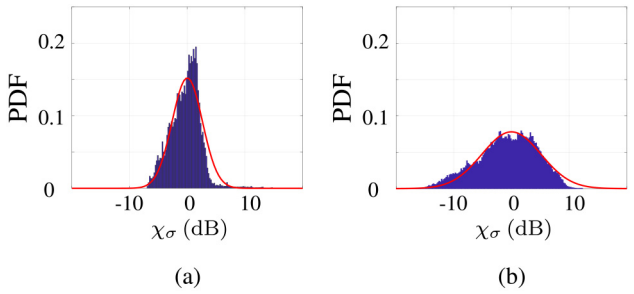

FIGURE 9. Log-normal shadow distribution for (a) the first and (b) the second segment of the two-slope PL model for the open field environment. The blue histogram indicates the PDF of the measurement data and the red line the fitted Gaussian distribution.

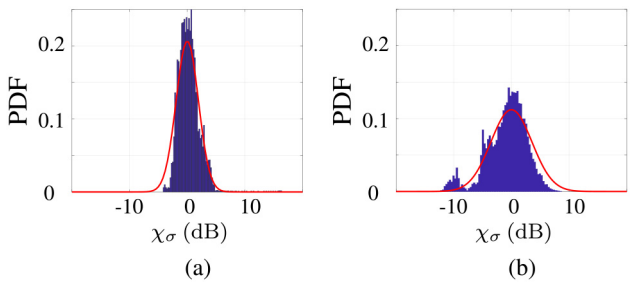

FIGURE 10. Log-normal shadow distribution for (a) the first and (b) the second segment of the two-slope PL model for the hilly terrain with cutting environment. The blue histogram indicates the PDF of the measurement data and the red line the fitted Gaussian distribution.

scale fading parameters include the Rician k-factor, the rms delay spread and the rms Doppler frequency spread. We investigated the noise level on a snapshot bases and applied a noise-power threshold at 3 dB above noise level to eliminate noise which could be mistaken as MPCs. Based on the stationarity assumptions we derive the parameters with

a frequency window $f_{\text{stat}} = 120\,\text{MHz}$ and with a time window $t_{\text{stat}} = 65.5\,\text{ms}$ represented by $I = 1537$ frequency bins $J = 64$ time snapshots, respectively.

We model time-variant behavior stochastic channel parameters in relation to the varying distance between Tx and Rx. The following derivation of model parameters is based on the three analyzed data sets. In comparison to Fig. 5 and 6 we extended the data sets to distances decreasing from $d_{\text{TR}} = 1000\,\text{m}$ to $d_{\text{TR}} = 5\,\text{m}$ when the Tx and Rx are next to each other and increasing from $d_{\text{TR}} = 5\,\text{m}$ again to $d_{\text{TR}} = 1000\,\text{m}$. The models cover three major railway environments: railway station, open field and hilly terrain with cutting.

A. PATH LOSS AND SHADOW FADING

The relation between the accumulated received power P_{R} for all delays τ of the PDP at time t and the transmitted Power P_{T} results in the

$$\text{PL}(t) = \frac{P_{\text{T}}}{P_{\text{R}}} = \frac{P_{\text{T}}}{\sum_{\tau=0}^{I-1} P_h(\tau; t)}. \tag{7}$$

Larger railway infrastructure, buildings and hills may cause shadowing effects on the transmitted signal which leads to a vastly lower received power as for LOS conditions at the same distance between Tx and Rx. Due to the rather large size of the IO, the shadowing extends over a large number of snapshots. If the shadowing effect is Gaussian distributed around the mean value μ of the PL, we can apply a log-normal distribution with standard deviation σ for the shadow fading [49]. The simplest theoretical PL model, purely based on the distance d can be calculated as

$$\text{PL}(d_{\text{TR}}) = 10n\ \log\left(\frac{4\pi\, d_{\text{TR}}\, f_{\text{c}}}{c}\right). \tag{8}$$

Setting the path loss exponent $n = 2$, we obtain the FSPL. In all three sub-figures of Fig. 7 the FSPL is indicated as a red dashed line.

In addition to the FSPL model we apply the log-distance PL model with log-normal shadow fading distribution. $\text{PL}(d_{\text{TR}})$ is composed as the path loss $\text{PL}(d_0)$ at a reference distance d_0, n times the logarithm of the relation between the actual link distance d_{TR} and d_0 and a Gaussian distributed vector $\chi_\sigma = \mathcal{N}(0, \sigma^2)$ with a standard deviation σ [49]

$$\text{PL}(d_{\text{TR}}) = \text{PL}(d_0) + 10n\ \log\left(\frac{d_{\text{TR}}}{d_0}\right) + \chi_\sigma. \tag{9}$$

The log-distance PL model is split at $d_{\text{TR}} = 100\,\text{m}$ in a near region and a far region. In Fig. 7 the resulting two-slope model is shown for all three environments. In comparison to [28] we evaluated the large scale fading on more comprehensive data sets and, as mentioned in Section II-A, we considered the antennas differently. Therefore, we obtain slightly different values for the large scale parameters n and σ.

The PL evaluation of a railway station environment shows a strong dependency on the architecture of the station. In Fig. 7(a) we see the green and orange indicated measurements for distances of up to 200 m. If a platform roof is in between Tx and Rx at the height of the antennas, the LOS signal is attenuated by 6 dB to 8 dB (see orange marked measurements in Fig. 7(a)) and the PL exponent $n = 2.5$. In [28] we used only this maneuver with platform roof. Hence, the PL exponent for distances up to 200 m are identical. If no IO is attenuating the LOS signal, $n = 2$ for distances of up to 100 m. For the shunting yard area in front of the platforms, the PL indicated in green or magenta in Fig. 7(a) is heavily influenced by the dense overhead line and signaling system. Therefore, the PL exponent increases for larger distances to $n = 2.7$. In [28] only the measurement data indicated in magenta in Fig. 7(a) is considered. As a result, the PL exponent is increased from $n = 2.7$ to $n = 4$ in [28]. The resulting values of the standard deviation for the shadow fading distribution are similar with values of $\sigma = [2.7, 3.0]\text{dB}$ versus $\sigma = [2.6, 2.9]\text{dB}$ in [28].

The PL in the open field environment can be modeled as shown in Fig. 7(b); we plotted the measurement data of three maneuvers in green, orange and blue. Small PL variation around FSPL in the near region up to 100 m result in $n = 2$. Comparing the results with [28], we see a difference in the plotted measurement data especially for $d_{\text{TR}} < 30\,\text{m}$ due to different considerations of the antenna pattern. The measurement data in Fig. 7(b) indicated in green and orange is used in [28] as well. We fitted in both evaluations a PL model with $n = 2$ for $d_{\text{TR}} \leq 100\,\text{m}$. For the far region the variation in power increases and by considering the green, orange and blue marked measurement data, we receive a PL exponent $n = 2.4$ with standard deviation $\sigma = 5.0\,\text{dB}$. In [28] only the green marked measurement data is used, which leads to $n = 3.5$ and $\sigma = 5.7\,\text{dB}$.

We see in Fig. 7(c) that the PL for hilly terrain with cutting with Tx-Rx distances ranging from 20 to 60 m varies slightly more as for the open field environment. We assume that this variation is caused by the cutting and walls as shown in Fig. 2(c). Similar as for the open field environment, we see a difference in the plotted measurement data of both evaluations due to the antenna pattern. As a consequence, we set the PL exponent $n = 2$ which results in a standard deviation $\sigma = 1.9\,\text{dB}$ for $d_{\text{TR}} \leq 100\,\text{m}$ in comparison to $n = 2.1$ and $\sigma = 2.9\,\text{dB}$ in [28]. For larger distances the PL exponent increases to $n = 3.2$ and $\sigma = 3.6\,\text{dB}$ due to obstructed LOS conditions caused by hills. In [28] we modeled the measurement data more pessimistic with $n = 4.2$ and $\sigma = 3.9\,\text{dB}$.

The log-normal shadow fading distribution for railway station is shown in Fig. 8, (a) and (b) show the probability density function (PDF) for the first segment either for the constellation without a platform roof between Tx and Rx or with a roof. Fig. 8(c) shows the PDF for the second segment. In Fig. 9 and Fig. 10 we show the log-normal shadow distribution for the first and second segment for open field and hilly terrain with cutting environments. All log-normal shadow fading distributions are modeled by a

Gaussian distribution; the corresponding values for σ are listed together with the path loss exponent n in Table 3.

B. RICIAN K-FACTOR

An important stochastic parameter in a multipath propagation scenario is the Rician k-factor. If a dominant signal, e.g., the LOS signal is present, the small scale fading can be described by a Rician fading distribution. The relation between the dominant signal and the scattered signal is called the Rician factor or k-factor. If k goes to zero, i.e., no dominant signal is present, the small scale fading distribution changes from a Rice to a Rayleigh distribution.

In many measurement evaluations and channel models the k-factor is given as an average value for one environment over the whole measurement time. We show, that k varies significantly over time even if the environment is not changed. Therefore, we evaluate k over time for each environment. If we consider a narrow band evaluation, the superposition of the LOS signal amplitude and the amplitudes of all MPCs for each snapshot results in constructive and destructive interference [50]. Hence, the envelope of the resulting amplitude varies over time [21]. The k-factor estimation was performed according to [51] based on the moment-method presented in [52]. In the literature many different estimation methods can be found. We compared the moment-method estimation with a maximum likelihood estimation as presented in [53]. As the difference was negligible, we used the less complex moment-method estimation

$$k(t) = \frac{\sqrt{G_{\mathrm{a}}^2(t) - G_{\mathrm{v}}(t)}}{G_{\mathrm{a}}(t) - \sqrt{G_{\mathrm{a}}^2(t) - G_{\mathrm{v}}(t)}}. \tag{10}$$

The first moment is represented by

$$G_{\mathrm{a}}(t) = \mathrm{E}\Big[\big|P'_h(t)\big|^2\Big], \tag{11}$$

where $\mathrm{E}[x]$ denotes the expected value of x, or in other words the mean value. The second moment can be calculated as the variance of our input signal

$$G_{\mathrm{v}}(t) = \mathrm{var}\Big(\big|P'_h(t)\big|^2\Big) = \mathrm{E}\Big[\Big(\big|P'_h(t)\big|^2 - G_{\mathrm{a}}(t)\Big)^2\Big]. \tag{12}$$

We derived the input for the k-factor estimation $P'_h(t)$ as follows. First, we superimposed the complex amplitudes over all delay bins for each snapshot. Second, we applied a 40 λ moving averaging window to remove the large scale fading. By fixing the window size to a multiple of λ we consider the different relative velocities of the Tx and Rx trains in the three environments.

Fig. 11 shows the resulting cumulative distribution functions (CDFs) of the k-factor for each environment. We fitted a normal distribution to each CDF. In each environment, the estimated k-factor fits well to the fit; as an example, we show the fit for the open field environment indicated as red dotted line.

We relate the mean value of the time-variant k-factor to the distance between Tx and Rx. In this way we can derive model parameters for the small scale fading in a similar manner as for the large scale fading. We calculate $\bar{k}(d_{\mathrm{TR}}) = \mathrm{E}[k(d_{\mathrm{TR}(t)})]$ for 200 bins, equally spaced over the logarithmic distance $d_{\mathrm{TR}} \in [10, 1000]$m. For all three railway environments $\bar{k}(d_{\mathrm{TR}})$ is shown in Fig. 12. The orange and black dash-dotted lines hold for the railway station environment. We see a clear difference of $\bar{k}(d_{\mathrm{TR}})$ in the case of the obstructed LOS signal due to a roof indicated in black in comparison to the case where no platform roof was in between Tx and Rx indicated in orange. In both cases we observe a strong variation of the k-factor and a decreasing trend with increasing distance.

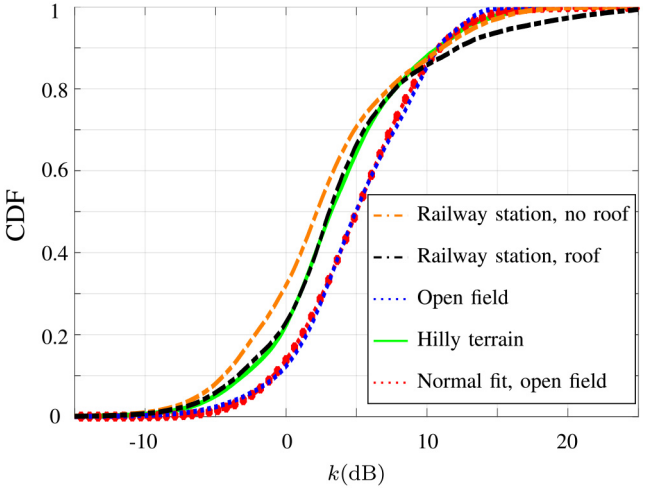

FIGURE 11. Empirical and fitted CDFs of the k-factor for railway environments.

The estimated k-factors of the open field and hilly terrain with cutting environment show a decrease from 15 dB at 25 m to 0 dB at 800 m. Above 800 m $\bar{k}$ is increasing again because of the low signal to noise ratio (SNR) of the MPCs. In both environments, the k-factor estimates vary strongly, where the k-factor for the open field environment is slightly higher as for hilly terrain with cutting. The lower average k-factor for the hilly terrain with cutting environment can be explained with the close and strongly reflecting walls and cuttings. The strong variations for $d_{\mathrm{TR}} \leq 25$ m and the drop for $\bar{k} < 0$ dB is caused by the variation of the azimuth antenna gain.

For all three environments the k-factor is very high in the distance range $d_{\mathrm{TR}} \in [10, 100]$m, which indicates a strong LOS signal. As the measurements were performed in rather straight track sections, a strong LOS signal and consequently a high k-factor is not surprising. Similar to the PL models we distinguish between two regions: The near region holds for distances between $d_{\mathrm{TR}} = 10$ m and $d_{\mathrm{TR}} = 100$ m and a far region from $d_{\mathrm{TR}} = 100$ m to $d_{\mathrm{TR}} = 1000$ m. To provide easy-to-use, but representative model parameters, we estimate an average Rician k-factor for each environment and region. The final parameters are summarized in Table 3.

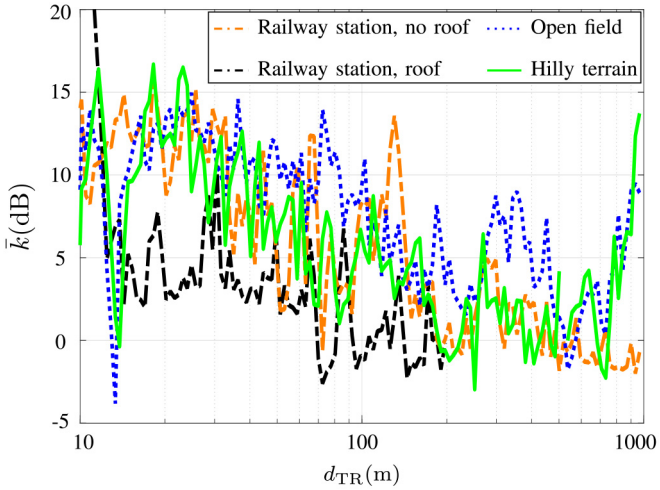

FIGURE 12. Distance-variant *k*-factor for railway environments.

C. DELAY SPREAD AND DOPPLER FREQUENCY SPREAD

The first and second central moments describe the mean and the variance of a function. Deriving the first and second central moment of the PDP we get the mean delay

$$\bar{\tau}(t) = \frac{\sum_{\tau=0}^{I-1} \tau(t) P_h(\tau; t)}{\sum_{\tau=0}^{I-1} P_h(\tau; t)} \tag{13}$$

and the rms delay spread

$$\sigma_\tau(t) = \sqrt{\frac{\sum_{\tau=0}^{I-1} (\tau(t) - \bar{\tau}(t))^2 P_h(\tau; t)}{\sum_{\tau=0}^{I-1} P_h(\tau; t)}}. \tag{14}$$

Similarly we derive the mean Doppler frequency

$$\bar{\nu}(t) = \frac{\sum_{\nu=-J/2}^{J/2-1} \nu(t) P_S(\nu; t)}{\sum_{\nu=-J/2}^{J/2-1} P_S(\nu; t)} \tag{15}$$

and the rms Doppler frequency spread based on the DSD

$$\sigma_\nu(t) = \sqrt{\frac{\sum_{\nu=-J/2}^{J/2-1} (\nu(t) - \bar{\nu}(t))^2 P_S(\nu; t)}{\sum_{\nu=-J/2}^{J/2-1} P_S(\nu; t)}}. \tag{16}$$

In the same way as for the *k*-factor we calculate a mean rms delay spread $\bar{\sigma}_\tau(d_{\mathrm{TR}})$ and a mean rms Doppler frequency spread $\bar{\sigma}_\nu(d_{\mathrm{TR}})$ for 200 bins, equally spaced over the logarithmic distance $d_{\mathrm{TR}} \in [10, 1000]$m. Fig. 13 shows $\bar{\sigma}_\tau(d_{\mathrm{TR}})$ and $\bar{\sigma}_\nu(d_{\mathrm{TR}})$ for railway station as orange dash-dotted lines, for open field as blue dotted lines and for hilly terrain as green solid lines. For the analysis of the rms delay spread in Fig. 13(a) and the rms Doppler frequency spread in Fig. 13(b), we distinguish between two regions: a near region for Tx-Rx distances between 10 m and 100 m, and a far region for Tx-Rx distances between 100 m and 1000 m.

The rms delay spread $\bar{\sigma}_\tau$ increases from 10 ns at $d_{\mathrm{TR}} = 10$ m to $\bar{\sigma}_\tau = 250$ ns at $d_{\mathrm{TR}} = 100$ m for the railway station environment. We can clearly see that the channel has a

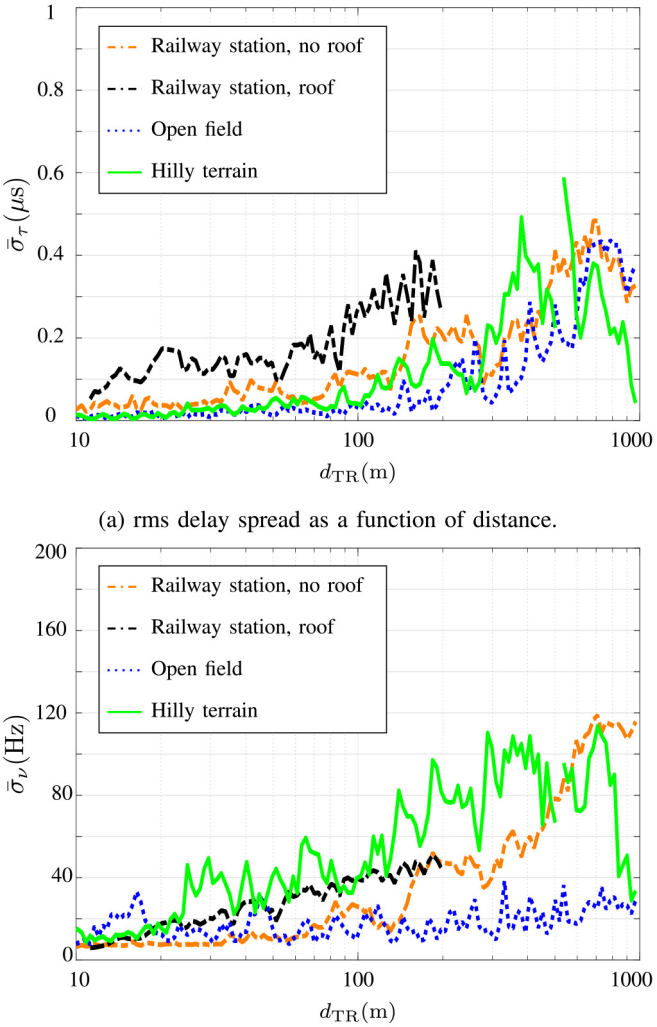

(a) rms delay spread as a function of distance.

(b) rms Doppler frequency spread as a function of distance.

FIGURE 13. Distance-variant rms delay and Doppler frequency spread for railway environments.

higher rms delay spread when a railway station has a platform roof. The lowest average delay spread $\bar{\sigma}_\tau = 20$ ns was estimated for the open field environment. The mean value for hilly terrain with cutting was estimated as $\bar{\sigma}_\tau = 32.7$ ns for the section of $d_{\mathrm{TR}} \in [10, 100]$m. In the far region of the railway station environment, the rms delay spread varies around $\bar{\sigma}_\tau = 276.7$ ns. In the open field environment, the rms delay spreads is relatively small and increases only for distances above 200 m with peaks at $\bar{\sigma}_\tau = 430$ ns. For all environments, the rms delay spread decreases for distances above 800 m because of the low SNR of the MPCs.

The rms Doppler frequency spread in Fig. 13(b) increases from 8 Hz to 40 Hz in the railway station environment. Again we can observe a clear difference for railway station environments with roof and without roof. Due to the regular appearing and fixed IOs, the open field environment shows a moderate variation with peaks at $\bar{\sigma}_\nu = 40$ Hz. The strongest variations and highest increase below $d_{\mathrm{TR}} = 100$ m are

TABLE 3. Stochastic channel parameters.

		d_0 [m]		P_0 [dBm]		n		σ [dB]		$\bar{k}$ [dB]		$\bar{\sigma}_\tau$ [ns]		$\bar{\sigma}_\nu$ [Hz]	
Environment \ Segment		1	2	1	2	1	2	1	2	1	2	1	2	1	2
Railway station	no roof	1	100	46.8	86.8	2	2.7	2.4	3.0	9.0	0.9	55.0	276.7	11.1	72.9
	roof	1	-	46.8	-	2.5	-	2.7	-	5.6	-	184.8	-	27.0	-
Open field		1	100	46.8	86.8	2	2.4	2.6	5.0	9.8	4.5	20.1	238.0	14.5	22.4
Hilly terrain		1	100	46.8	86.8	2	3.2	1.9	3.6	7.0	3.1	32.7	240.7	32.8	76.7

obtained for the hilly terrain with cutting environment. In the far region, $\bar{\sigma}_\nu$ increases strongly for the railway station environment to $\bar{\sigma}_\nu = 119$ Hz. The rms Doppler frequency spread remains constant for the open field environment. In the hilly terrain with cutting environment, $\bar{\sigma}_\nu$ continues increasing up to SI115Hz.

Similar as for the k-factor, we estimate average rms delay spread values and average rms Doppler frequency spread values for the near and the far region of all three environments and summarized the values in Table 3.

V. CONCLUSION

In this paper, we investigated the propagation channel for train-to-train (T2T) communications. We provided the stochastic description of the following five small and large scale fading parameters for three different environments as a function of the propagation distance: path loss (PL) exponents, log-normal shadow fading distributions, k-factors, root mean square (rms) delay spreads and rms Doppler frequency spreads. Our analysis is based on channel sounding data of an extensive T2T measurement campaign with two high speed trains traveling though three environments: railway station, open field and hilly terrain with cutting.

We investigated the stationarity behavior of the T2T propagation channel in time and frequency for wide-sense stationary (WSS) and uncorrelated scattering (US), respectively. The collinearity analysis showed quasi-stationarity behavior within a time window of $t_{\text{stat}} = 65.5$ ms. Furthermore, we found out that US can be assumed for the whole measurement bandwidth $f_{\text{stat}} = B = 120$ MHz.

Within the presented stationary regions we derived power delay profiles (PDPs) and Doppler spectral densities (DSDs). The PDP and DSD representations showed regularly occurring patterns of pronounced multipath components (MPCs) in all three environments. The MPCs shown in the PDP plots reflect well the underlying geometry of transmitter (Tx), receiver (Rx) and interacting objects. The MPCs can be well explained by cross bridges, buildings and by the railway infrastructure, e.g., overhead line masts occurring at regular intervals. Furthermore, MPCs caused by the train bodies could be identified. The Doppler frequency variations of the line of sight signal and the MPCs shown in the DSD figures are explained by the movement of the Tx and Rx.

Based on the PDP we plotted the measured PL and derived large scale fading parameters. We fitted two-slope log-distance PL models for propagation distances up to 1000 m and derived the path loss exponent n for all three environments. The first segment of the two-slope model was derived for a near region with $d_{\text{TR}} \in [10, 100]$m, the second segment was derived for a far region with $d_{\text{TR}} \in (100, 1000]$m. In the railway station environment we differentiate between measurements performed with or without platform roof. The standard deviation σ of the log-normal shadow fading distribution was derived for all environments and segments of the two-slope log-distance PL models.

Small scale fading parameters like the time-variant k-factor, the rms time-variant delay and the rms time-variant Doppler frequency spread have been analyzed. We related the time-variant behavior of the parameters to the propagation distance between Tx and Rx. In this way, we derived an average k-factor $\bar{k}$, an average rms delay spread $\bar{\sigma}_\tau$ and an average rms Doppler frequency spread $\bar{\sigma}_\nu$ for the same distance segments as for the large scale fading.

REFERENCES

[1] J. Moreno, J. Riera, L. de Haro, and C. Rodríguez, "A survey on future railway radio communications services: Challenges and opportunities," *IEEE Commun. Mag.*, vol. 53, no. 10, pp. 62–68, Oct. 2015.

[2] (2020). *S2R*. [Online]. Available: http://www.shift2rail.org

[3] A. Lehner, C. R. García, and T. Strang, "On the performance of TETRA DMO short data service in railway VANETs," *Wireless Pers. Commun.*, vol. 69, no. 4, pp. 1647–1669, 2013.

[4] C. R. Garcia, A. Lehner, T. Strang, and K. Frank, "Channel model for train to train communication using the 400 MHz band," in *Proc. IEEE Veh. Technol. Conf. (VTC Spring)*, May 2008, pp. 3082–3086.

[5] A. Lehner, C. R. García, T. Strang, and O. Heirich, "Measurement and analysis of the direct train to train propagation channel in the 70 cm UHF-band," in *Communication Technologies for Vehicles*. Heidelberg, Germany: Springer, 2011, pp. 45–57.

[6] X. Wang, L. Liu, T. Tang, and W. Sun, "Enhancing communication-based train control systems through train-to-train communications," *IEEE Trans. Intell. Transp. Syst.*, vol. 20, no. 4, pp. 1544–1561, Apr. 2019.

[7] X. Wang, L. Liu, L. Zhu, and T. Tang, "Train-centric CBTC meets age of information in train-to-train communications," *IEEE Trans. Intell. Transp. Syst.*, vol. 21, no. 10, pp. 4072–4085, Oct. 2020.

[8] P. Liu, B. Ai, Z. Zhong, and X. Zhou, "A novel train-to-train communication model design based on multihop in high-speed railway," *Int. J. Antennas Propag.*, vol. 2012, pp. 1–9, Dec. 2012. [Online]. Available: http://www.hindawi.com/journals/ijap/2012/475492/

[9] A. A. Gómez *et al.*, "Performance analysis of ITS-G5 for smart train composition coupling," in *Proc. 16th Int. Conf. Intell. Transp. Syst. Telecommun. (ITST)*, Oct. 2018, pp. 1–7.

[10] P. Unterhuber, S. Sand, U.-C. Fiebig, and B. Siebler, "Path loss models for train-to-train communications in typical high speed railway environments," *IET Microw. Antennas Propag.*, vol. 12, no. 4, pp. 492–500, Mar. 2018.

[11] P. Unterhuber, A. Lehner, and F. de Ponte Müller, "Measurement and analysis of ITS-G5 in railway environments," in *Communication Technologies for Vehicles*, S. Sebastian, Ed. Cham, Switzerland: Springer, 2016, pp. 62–73. [Online]. Available: http://link.springer.com/10.1007/978-3-319-38921-9_7

[12] K. Guan, Z. Zhong, B. Ai, and T. Kürner, "Propagation measurements and analysis for train stations of high-speed railway at 930 MHz," *IEEE Trans. Veh. Technol.*, vol. 63, no. 8, pp. 3499–3516, Oct. 2014.

[13] K. Guan, Z. Zhong, B. Ai, and T. Kürner, "Propagation measurements and modeling of crossing bridges on high-speed railway at 930 MHz," *IEEE Trans. Veh. Technol.*, vol. 63, no. 2, pp. 502–517, Feb. 2014.

[14] L. Zhou, F. Luan, S. Zhou, A. F. Molisch, and F. Tufvesson, "Geometry-based stochastic channel model for high-speed railway communications," *IEEE Trans. Veh. Technol.*, vol. 68, no. 5, pp. 4353–4366, May 2019.

[15] L. Zhou, Z. Yang, F. Luan, A. F. Molisch, F. Tufvesson, and S. Zhou, "Dynamic channel model with overhead line poles for high-speed railway communications," *IEEE Antennas Wireless Propag. Lett.*, vol. 17, pp. 903–906, 2018.

[16] B. Ai *et al.*, "Challenges toward wireless communications for high-speed railway," *IEEE Trans. Intell. Transp. Syst.*, vol. 15, no. 5, pp. 2143–2158, Oct. 2014.

[17] C.-X. Wang, A. Ghazal, B. Ai, Y. Liu, and P. Fan, "Channel measurements and models for high-speed train communication systems: A survey," *IEEE Commun. Surveys Tuts.*, vol. 18, no. 2, pp. 974–987, 2nd Quart., 2016.

[18] Y. Liu, C.-X. Wang, and J. Huang, "Recent developments and future challenges in channel measurements and models for 5G and beyond high-speed train communication systems," *IEEE Commun. Mag.*, vol. 57, no. 9, pp. 50–56, Sep. 2019.

[19] B. Ai, A. F. Molisch, M. Rupp, and Z.-D. Zhong, "5G key technologies for smart railways," *Proc. IEEE*, vol. 108, no. 6, pp. 856–893, Jun. 2020.

[20] A. Paier, L. Bernadó, J. Karedal, O. Klemp, and A. Kwoczek, "Overview of vehicle-to-vehicle radio channel measurements for collision avoidance applications," in *Proc. IEEE 71st Veh. Technol. Conf.*, May 2010, pp. 1–5.

[21] L. Bernadó, T. Zemen, F. Tufvesson, A. F. Molisch, and C. F. Mecklenbräuker, "Time- and frequency-varying *K*-factor of non-stationary vehicular channels for safety-relevant scenarios," *IEEE Trans. Intell. Transp. Syst.*, vol. 16, no. 2, pp. 1007–1017, Apr. 2015.

[22] L. Bernadó, T. Zemen, F. Tufvesson, A. F. Molisch, and C. F. Mecklenbräuker, "Delay and doppler spreads of nonstationary vehicular channels for safety-relevant scenarios," *IEEE Trans. Veh. Technol.*, vol. 63, no. 1, pp. 82–93, Jan. 2014.

[23] A. F. Molisch, F. Tufvesson, J. Karedal, and C. F. Mecklenbräuker, "A survey on vehicle-to-vehicle propagation channels," *IEEE Wireless Commun.*, vol. 16, no. 6, pp. 12–22, Dec. 2009.

[24] C. F. Mecklenbräuker *et al.*, "Vehicular channel characterization and its implications for wireless system design and performance," *Proc. IEEE*, vol. 99, no. 7, pp. 1189–1212, Jul. 2011.

[25] D. W. Matolak, "Modeling the vehicle-to-vehicle propagation channel: A review," *Radio Sci.*, vol. 49, no. 9, pp. 721–736, Sep. 2014.

[26] W. Viriyasitavat, M. Boban, H.-M. Tsai, and A. Vasilakos, "Vehicular communications: Survey and challenges of channel and propagation models," *IEEE Veh. Technol. Mag.*, vol. 10, no. 2, pp. 55–66, Jun. 2015.

[27] P. Unterhuber *et al.*, "A survey of channel measurements and models for current and future railway communication systems," *Mobile Inf. Syst.*, vol. 2016, pp. 1–14, Jul. 2016. [Online]. Available: http://dx.doi.org/10.1155/2016/7308604

[28] P. Unterhuber, I. Rashdan, M. Walter, and T. Kürner, "Path loss models and large scale fading statistics for C-band train-to-train communication," in *Proc. 14th Eur. Conf. Antennas Propag. (EuCAP)*, Apr. 2020, pp. 1–5.

[29] P. Unterhuber, M. Walter, N. Schneckenburger, and T. Kürner, "Joint delay and doppler frequency estimation for scatterer localization in railway environments," in *Proc. 13th Eur. Conf. Antennas Propag. (EuCAP)*, Mar. 2019, pp. 1–5.

[30] P. Unterhuber, M. Walter, and T. Kürner, "Influence of railway infrastructure on train-to-train communications," in *Proc. 15th Eur. Conf. Antennas Propag. (EuCAP)*, Apr. 2021, pp. 1–5.

[31] P. Unterhuber *et al.*, "Wide band propagation in train-to-train scenarios—Measurement campaign and first results," in *Proc. 11th Eur. Conf. Antennas Propag. (EuCAP)*, Mar. 2017, pp. 3356–3360.

[32] Huber+Suhner. (2021). *Datasheet 1399.99.0120*. [Online]. Available: https://ecatalog.hubersuhner.com/media/documents/datasheet/en/pdf/84071811?s=true

[33] T. Domínguez-Bolaño, "Design and evaluation of new waveforms for high mobility communications," M.S. thesis, Dept. Inf. Technol. Mobile Netw. Commun., Universidade da Coruña, Ferrol, Spain, Sep. 2018.

[34] TG-Trains. (2011). *Video Roma Termini—Napoli Centrale via AV*. [Online]. Available: http://www.tg-trains.com/alta-velocita.html

[35] P. A. Bello, "Characterization of randomly time-variant linear channels," *IEEE Trans. Commun. Syst.*, vol. 11, no. 4, pp. 360–393, Dec. 1963.

[36] R. Kattenbach, *Charakterisierung Zeitvarianter Indoor-Funkkanäle Anhand Ihrer System- Und Korrelationsfunktionen*. Kassel, Germany: Shaker-Verlag, 1997.

[37] A. Molisch, *Wireless Communications*, 2nd ed. New York, NY, USA: Wiley, 2011.

[38] R. He *et al.*, "Characterization of quasi-stationarity regions for vehicle-to-vehicle radio channels," *IEEE Trans. Antennas Propag.*, vol. 63, no. 5, pp. 2237–2251, May 2015. [Online]. Available: http://ieeexplore.ieee.org/document/7038157/

[39] F. J. Harris, "On the use of windows for harmonic analysis with the discrete Fourier transform," *Proc. IEEE*, vol. 66, no. 1, pp. 51–83, Jan. 1978.

[40] G. Matz, "On non-WSSUS wireless fading channels," *IEEE Trans. Wireless Commun.*, vol. 4, no. 5, pp. 2465–2478, Sep. 2005. [Online]. Available: http://ieeexplore.ieee.org/document/1532230/

[41] B. H. Fleury, "An uncertainty relation for WSS processes and its application to WSSUS systems," *IEEE Trans. Commun.*, vol. 44, no. 12, pp. 1632–1634, Dec. 1996.

[42] D. Czaniera *et al.*, "Investigation on stationarity of V2V channels in a highway scenario," in *Proc. 13th Eur. Conf. Antennas Propag. (EuCAP)*, 2019, pp. 1–5.

[43] A. Paier, "The vehicular radio channel in the 5 GHz band," Ph.D.dissertation, Dept. Inst. Telecommun. High Frequency Technol., Technischen Universitat Wien, Vienna, Austria, Oct. 2010.

[44] C. A. Gutiérrez, J. T. Gutiérrez-Mena, J. M. Luna-Rivera, D. U. Campos-Delgado, R. Velázquez, and M. Pätzold, "Geometry-based statistical modeling of non-WSSUS mobile-to-mobile rayleigh fading channels," *IEEE Trans. Veh. Technol.*, vol. 67, no. 1, pp. 362–377, Jan. 2018.

[45] G. A. Gehring, M. Steinbauer, I. Gaspard, and M. Grigat, "Empirical channel stationarity in urban environment," in *Proc. 4th Eur. Pers. Mobile Commun. Conf.*, Vienna, Austria, 2001, pp. 1–6.

[46] L. Bernadó, *Non-Stationarity in Vehicular Wireless Channels*. Vienna, Austria: FTW Forschungszentrum Telekommunikation Wien GmbH, 2012.

[47] L. Bernadó, T. Zemen, F. Tufvesson, A. F. Molisch, and C. F. Mecklenbräuker, "The (in-) validity of the WSSUS assumption in vehicular radio channels," in *Proc. IEEE 23rd Int. Symp. Pers. Indoor Mobile Radio Commun. (PIMRC)*, 2012, pp. 1757–1762.

[48] M. Walter, D. Shutin, and A. Dammann, "Time-variant doppler PDFs and characteristic functions for the vehicle-to-vehicle channel," *IEEE Trans. Veh. Technol.*, vol. 66, no. 12, pp. 10748–10763, Dec. 2017. [Online]. Available: http://ieeexplore.ieee.org/document/7964694/

[49] T. S. Rappaport, *Wireless Communications: Principles and Practice* (Prentice Hall Communications Engineering and Emerging Technologies Series). Upper Saddle River, NJ, USA: Prentice-Hall PTR, 2002.

[50] T. Zhou, C. Tao, L. Liu, and Z. Tan, "Ricean K-factor measurements and analysis for wideband radio channels in high-speed railway U-shape cutting scenarios," in *Proc. IEEE 79th Veh. Technol. Conf. (VTC Spring)*, Seoul, South Korea, May 2014, pp. 1–5. [Online]. Available: http://ieeexplore.ieee.org/document/7023077/

[51] R. He, Z. Zhong, B. Ai, J. Ding, Y. Yang, and A. F. Molisch, "Short-term fading behavior in high-speed railway cutting scenario: Measurements, analysis, and statistical models," *IEEE Trans. Antennas Propag.*, vol. 61, no. 4, pp. 2209–2222, Apr. 2013.

[52] L. J. Greenstein, D. G. Michelson, and V. Erceg, "Moment-method estimation of the Ricean K-factor," *IEEE Commun. Lett.*, vol. 3, no. 6, pp. 175–176, Jun. 1999.

[53] Y. Chen and N. C. Beaulieu, "Maximum likelihood estimation of the K factor in Ricean fading channels," *IEEE Commun. Lett.*, vol. 9, no. 12, pp. 1040–1042, Dec. 2005.

PAUL UNTERHUBER (Member, IEEE) received the M.Sc. degree in electrical engineering and the M.Sc. degree in engineering and business from the Graz University of Technology, Graz, Austria, in 2013 and 2014, respectively.

Since 2015, he has been with the Institute of Communications and Navigation, German Aerospace Center, Oberpfaffenhofen, Germany. He has been participating in several national and international research projects, e.g., SBDist, V2X-DuRail, Roll2Rail, and X2-Rail. His research interests are on channel sounding, propagation, and modeling with a focus on train-to-train communications. He is currently a Voting Member of IEEE 802.11 and contributing to the IEEE 802.11bd and ETSI RT JTFIR standardization bodies.

MICHAEL WALTER (Senior Member, IEEE) received the Dipl.-Ing. and Dr.-Ing. degrees in electrical engineering from Ulm University, Germany, in 2008 and 2015, respectively.

Since 2009, he has been a member of the scientific staff with the Institute of Communications and Navigation, German Aerospace Center, Oberpfaffenhofen, Germany, where he gained extensive experience in organizing and conducting numerous measurement campaigns for vehicular and aeronautical research. He was a Visiting Scholar with the School of Electrical and Computer Engineering, Georgia Institute of Technology in 2014. His research interests include wireless communications, modeling of mobile-to-mobile channels, and channel coding.

Dr. Walter was the recipient of the IEEE/AIAA David Lubkowski Memorial for Advancement in Digital Avionics Best Paper Award of the 29th DASC in 2011.

UWE-CARSTEN FIEBIG (Senior Member, IEEE) received the Dipl.-Ing. degree in electrical engineering with a focus on communication technology from the Technical University of Munich, Germany, in 1987, and the Dr.-Ing. degree from the University of Kaiserslautern, Germany, in 1993.

He joined the Institute of Communications and Navigation, German Aerospace Center (DLR), Oberpfaffenhofen, Germany, in 1988. From 1999 to 2004, he was a Guest Professor with Johannes Kepler University, Linz, Austria. From 1999 to 2010, he was a Lecturer with the University of Ulm, Germany, where he has been an Honorary Professor since 2011 and teaches satellite communication and navigation. At DLR, he is responsible for research in aeronautical and vehicular communications, multisensor navigation, and swarm exploration. A special focus is on propagation for aircraft, drones, ships, cars, and trains. He is a (co)author of over 150 publications including over 35 journal papers.

Prof. Fiebig received several best paper awards from the Digital Avionics Systems Conference and the European Conference on Antennas and Propagation and is the Co-Editor of the *IEEE Vehicular Technology Magazine*. He is a member of the European Association on Antennas and Propagation, the Verband der Elektrotechnik, Elektronik und Informationstechnik (VDE), and the IEEE VTS Committee on Drones.

THOMAS KÜRNER (Fellow, IEEE) received the Dipl.-Ing. degree in electrical engineering and the Dr.-Ing. degree from the University of Karlsruhe, Germany, in 1990 and 1993, respectively.

From 1990 to 1994, he was with the Institut für Höchstfrequenztechnik und Elektronik, University of Karlsruhe working on wave propagation modeling, radio channel characterization, and radio network planning. From 1994 to 2003, he was with the Radio Network Planning Department at the headquarters of the GSM 1800 and UMTS operator E-Plus Mobilfunk GmbH & Co. KG, Düsseldorf, where he was a Team Manager of radio network planning support responsible for radio network planning tools, algorithms, processes, and parameters from 1999 to 2003. Since 2003, he has been a Full University Professor for Mobile Radio Systems with Technische Universität Braunschweig. In 2012, he was a Guest Lecturer with the Telecommunications Graduate Initiative, Dublin City University, Ireland.

Prof. Kürner received the Neal-Shephard Award of the IEEE Vehicular Technology Society in 2019. He is chairing the IEEE 802.15 Standing Committee THz. He was also the Chair of IEEE 802.15.3d TG 100G, which developed the worldwide first wireless communications standard operating at 300 GHz. He is also the Project Coordinator of the H2020-EU-Japan Project ThoR ("Terahertz end-to-end wireless systems supporting ultra-high data rate applications") and the Coordinator of the German DFG-Research Unit FOR 2863 Meteracom ("Metrology for THz Communications"). He has been a member of the Board of Directors of the European Association on Antennas and Propagation since 2016 and a Distinguished Lecturer of the IEEE Vehicular Technology Society since 2020.